Chapter 6

Spectrographs

In this chapter, the basic principles of spectrograph design are reviewed. Both low order (low–resolution) and high order (high resolution echelle configurations) are presented. Derivations of the optical principles are not given, but only results that are central to a basic understanding of the dispersion relations, the spectral purity, and the resolution of the spectra. Though dispersion of the light can be obtained via prisms or gratings, only the properties of gratings are discussed (since they are most common).

Also discussed are the blaze function, throughput, resolving power, instrumental spread function, pixel sample rate, and the so–called "resolution element". The relationship between the detected counts and the observed flux is presented. Extraction and calibration of spectroscopic data is reserved for Chapter 7. Further details on optics, spectrographs, diffraction gratings, and the principles of diffraction gratings can be found in Hecht & Zajac (1974), Shroeder (1987), and Gray (1992).

6.1 The spectrograph

The basic components of a spectrograph are the entrance slit, a collimator, a grating or prism, a camera, and the detector. It is common for the dispersive element in modern spectrographs to be a grating. As shown in Figure 6.1, the light first enters the slit. The slit (1) is located at the focal point of the telescope and the light beam is diverging as the light path exits the slit. The light is then collimated by the collimator (2), which is located at a distance f_{coll} from the slit. The collimated light then strikes the disperser, which is a ruled grating (3). The grating is tilted with respect to the incoming light path. The reflected light is then focused by a camera (4) with focal length f_{cam} onto the detector (5).

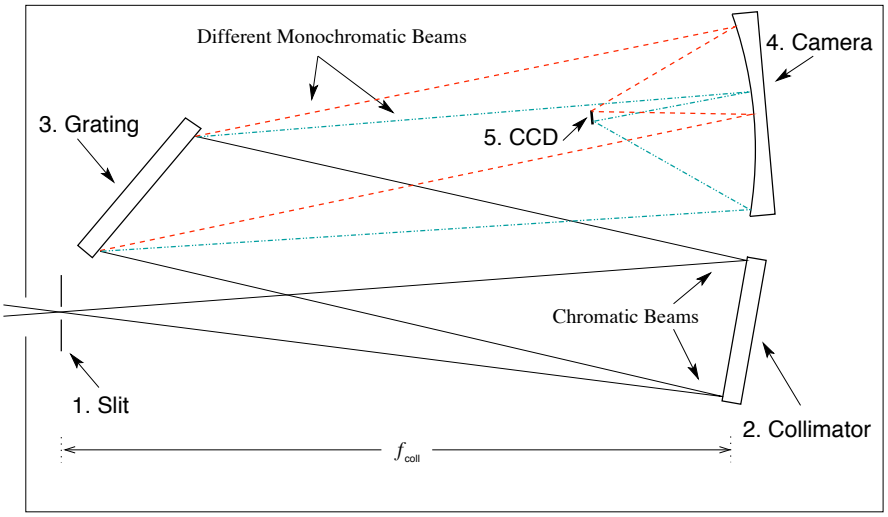

Figure 6.1: A schematic of a grating spectrograph showing the optical layout and light path from slit to detector. The distance from the collimator is the collimator focal length, f_{coll}, and the distance from the camera mirror to the detector is f_{cam}. The light is focused by the telescope on the plane of the slit. The chromatic beam (solid lines) then diverges until it is parallelized by the collimator. After the light reflects off the grating, the light is organized into monochromatic beams with different wavelengths (dash–dash and dash–dot lines) due to diffraction; each monochromatic beam propagates in a unique direction. These beams are then focused by the camera at different spatial locations along the detector, forming the spectrum.

Modern detectors are usually charged coupled devices, or CCDs, with finite pixels, which results in a discretized sampling of the dispersed light. The spectrum has a dispersion direction and a spatial direction. The spatial direction will be governed by the collimator and camera focal lengths, and the dispersion will be governed by both the grating properties and the collimator and camera focal lengths. There are secondary effects governing the spatial and dispersion charactersitics of the spectrum, including the stability of the image of the source on the slit (guiding), the atmospheric turbulence (seeing), and the angle of the slit with respect to the parallactic angle (affecting chromatic dispersion of the image).

6.2 The seeing disk

For a point source, the physical radius of the image in the telescope focal plane (at the slit) is governed by the combined effects of guiding errors and atmospheric "seeing" conditions (the atmospheric turbulence along the sight line to the object and in the environment of the observatory and telescope dome). Guiding errors and seeing cause a point source to appear as if it has an angular extension on the sky in that the image of the object is "blurred". Seeing is expressed in seconds of arc [arcsec].

To a good approximation, the resulting surface brightness pattern of the flux of the image in the focal plane of the telescope is an axial symmetric Gaussian,

$$\mu_\lambda(r) = \frac{1}{2\pi\,\sigma_\lambda^2} \exp\left\{-\frac{r^2}{2\sigma_\lambda^2}\right\}, \tag{6.1}$$

in units of [erg sec^{-1} cm^{-2} Å^{-1} mm^{-2}], where r is the physical coordinate in the telescope focal plane (measured in milimmeters [mm]) with $r = 0$ the peak, $\mu(0)$, and where σ_λ is the profile disperion width. The magnitude of σ_λ is wavelength dependent. Atmospheric dispersion and refraction decreases with increasing wavelength. Note that $\mu_\lambda(r)$ is defined such that $\int_{-\infty}^{\infty} \mu_\lambda(r)dr = 1$. Eq. 6.1 is often called the point spread function of the telescope image.

The seeing is measured from the full–width half–maximum, $\text{FWHM}_\lambda = 2.35\sigma_\lambda$, of the telescope point spread function. The conversion between the aparent angle subtendend by the image on the sky and the physical size of the image in the telescope focal plane is given by the telescope plate scale

$$\theta_{\rm ps} = \frac{1}{f_{\rm T}}, \tag{6.2}$$

in units of [radians mm^{-1}] where $f_{\rm T}$ is the effective focal length of the telescope optics. The effective focal length is often quoted in millimeters [mm] and is on the order of 10^3 to 10^4.

Under the conditions of excellent guiding, the σ_λ of the imaged point source object will be dominated by atmospheric seeing; thus, $\mu_\lambda(r)$ is often refered to as the "seeing disk". The full–width half–maximum of a point source seeing disk is the quantity quoted to quantify the seeing conditions. If the measured radius of the seeing disk is σ_λ [mm], then the seeing is

$$\theta_{\sigma_\lambda} = (2.35\sigma_\lambda)\,\theta_{\rm ps} = 206,265\left(\frac{2.35\,\sigma_\lambda}{f_{\rm T}}\right), \tag{6.3}$$

in units of [arcsec] where the factor 206,265 is the conversion [arcsec radian^{-1}]. Most astronomical facilities strive to deliver seeing on the order of 0.5 [arcsec]. Adaptic optics can significantly reduce θ_{σ_λ}.

6.3 Slits

The slit is an aperture that lies in the focal plane of the telescope and receives the chromatic seeing disk of the focused image. As illustrated in Figure 6.2, slits are characterized by their physical width, w, and height, h, often in units of millimeters [mm]. For a point source, the width of the slit is chosen such that $w \simeq 3\sigma_\lambda$ and is positioned roughly at the center point along the slit height. Since the seeing disk is wavelength dependent, it is wise to perform the centering at a wavelength near the spectral region of scientific interest.

The slit height is chosen such that a desired amount of sky light is allowed to pass through the spectrograph adjacent to the image of the object. The sky

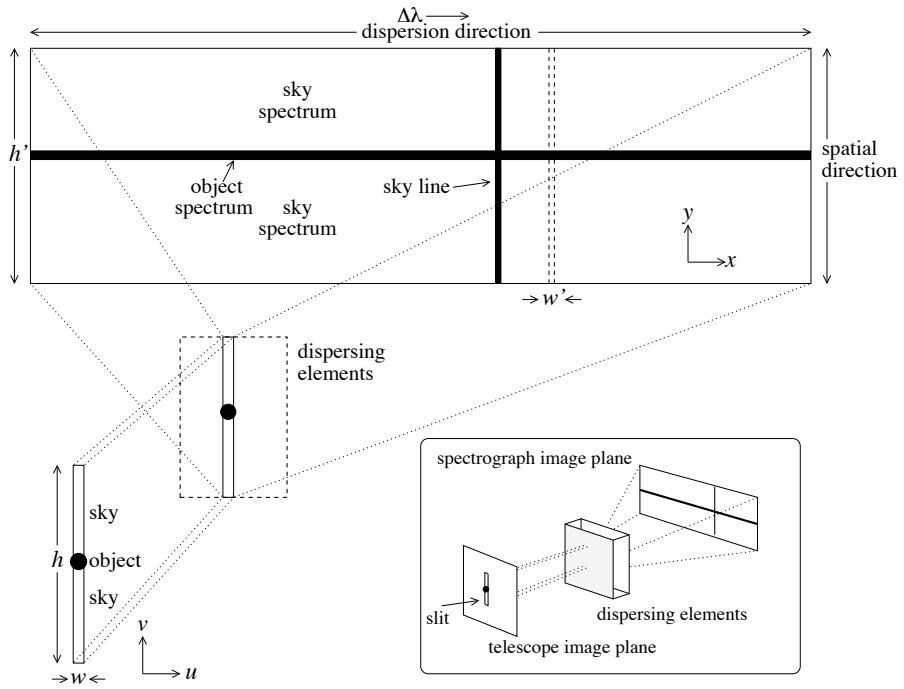

Figure 6.2: A schematic of the spatial and dispersion mapping of the slit for a point source object. The slit has width w in the u coordinate and height h in the v coordinate and lies in the telescope image plane. Sky passes through the slit along the slit height. The dispersing elements of the spectrograph disperse the light along the x coordinate (dispersion direction) in the spectrograph image plane. In the slit height direction, the object and sky are imaged in the y coordinate (spatial direction). In the spectrograph image plane, the slit width has physical projection w' in the x coordinate and the slit height has physical projection h' in y coordinate. Sky emission lines are imaged along the y coordinate (mapped along the slight height), but they are dispersed to various x positions depending upon their wavelength.

not only contributes a smooth background (unwanted photons), but also narrow emission and both narrow and broad absorption lines. It is desirable to obtain a good sampling of these quantities independent of the object in order that they can eventually be removed from the object spectrum. The configuration $h \gg w$ is known as long slit mode. In certain configurations, such as with echelle spectrogaphs (§ 6.6), a shortened slit is employed.

The angular projection of the slit width on the sky is w times the plate scale

$$\theta_w = w\,\theta_{\rm ps} = 206,265\,\left(\frac{w}{f_{\rm T}}\right)\,, \tag{6.4}$$

in units of [arcsec], where w and $f_{\rm T}$ are in [mm]. Similarly, the angular projection of the slit height on the sky is $\theta_h = 206,265\,(h/f_{\rm T})$. In practice, observatories may provide the option to set the slit width and/or height in units of [arcsec] rather than in [mm]. Clearly the chosen slit angular width should be on the order of the seeing disk σ_λ in order to minimize loss of light (slit too narrow)

or compromise the purity of the object light (slit too wide).

Also illustrated in Figure 6.2 is a schematic of the mapping of light onto the image plane of the spectrograph. The chromatic light entering the slit passes to the dispersing elements and is wavelength dispersed along the x coordinate of the spectrograph image plane. The x coordinate is known as the dispersion direction. In the y coordinate, the object and sky are not dispersed; they are imaged. Thus, the y coordinate is known as the spatial direction; a constant y at a given given x (vertical cut along the spectrograph image plane) is a monochromatic image of the slit. A y spatial cut of the spectrum is known as the aperture profile or the illumination profile. In the spectrograph image plane, the slit width has physical size w' in x coordinates and the slit height has physical size h' in y coordinates.

In the spectrograph image plane, the (i) plate scales, θ_x and θ_y, (ii) dispersion relationship $d\lambda/dx$, and (iii) magnification w'/w in x, are dependent upon both the optical and dispersive properties of the spectrograph. The magnification in y is independent of the dispersion, depending only upon the optical elements, such that $h'/h = f_{cam}/f_{coll}$.

6.4 Diffraction gratings

A typical grating can be characterized by equally space grooves, called facets. Consider a grating of length L, as illustrated in Figure 6.3, with facet widths s and with center–to–center spacings d, with the condition $d > s$. The ratio L/d gives the number of facets, N_f, on the grating. It is important to keep in mind that for the following discussion, all relations apply to a monochromatic diffracted light beam (even though the incoming light is chromatic). The full repsonse behavior of a spectrograph is obtained by considering the combined behavior of the diffracted monochromatic beams over the wavelength range of the incoming chromatic beam.

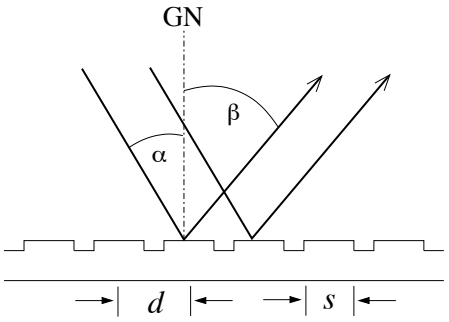

Figure 6.3: A schematic of a reflection grating showing the individual grooves, or facets. The facets are characterized by their edge–to–edge lengths, s, and center–to–center separation d. The incoming light has an angle of incidence α, measured with respect to the grating normal, GN. Intereference of the reflected wave fronts yields a diffraction angle, β, which is a function of wavelength phase differences (Eq. 6.5).

For a specific spectrograph design, the grating is tilted so that the angle of incidence of the incoming collimated chromatic light is α with respect to the grating normal. After interaction with the grating, the light is diffracted at wavelength dependent angles, β; there is a unique value of β for each wavelength, λ, that depends upon wavelength phase differences. For reflection gratings, as shown in Figure 6.3, β is defined to be negative.

As discussed in the following sections, there are two interference patterns that govern the angular dependence of the intensity function (fraction of transmitted intensity) at each wavelength. The first is due to phase differences between the centers of adjacent facets, φ_{cc}. The second is due to phase differences between the center and edge of each facet, φ_{ce}.

6.4.1 The grating equation

Light with wavelength λ is "reflected" at an angle of diffraction that corresponds to constructive interference, or facet center to facet center phase differences of $\varphi_{cc} = n\pi$. The relationship between the diffraction angle and the wavelength is given by the grating equation,

$$\frac{n\lambda}{d} = \sin\alpha + \sin\beta, \tag{6.5}$$

where the integer n is called the diffraction order. The angular dispersion with wavelength is obtained by differentiating Eq. 6.5,

$$\frac{d\beta}{d\lambda} = \frac{n}{d\cos\beta} = \frac{\sin\alpha + \sin\beta}{\lambda\cos\beta}, \tag{6.6}$$

from which it is clear that the angular dispersion increases with larger n and smaller d.

The behavior of the grating equation (Eq. 6.5) is illustrated in Figure 6.4, for orders $n = 1$, 2, and 3 for a grating with $1/d = 1200$ facets mm^{-1} for an incident angle $\alpha = 40°$. For $n = 0$, there is no disperion and all wavelengths of the chromatic incident beam are diffracted at angle $\beta = -\alpha$. As n increases, the dispersion increases. For the example grating, if one wished to observe a wavelengths in the regime of 6000 Å, the camera would need to be placed at $\beta = 5°$ for $n = 1$ (lowest) dispersion or $\beta = 55°$ for $n = 2$ (higher) dispersion.

6.4.2 Free spectral range

As can be seen in Figure 6.4, the camera can be placed to capture the spectrum for any desired order. However, there are multiple $n\lambda$ that satisfy Eq. 6.5 for a given β. Thus, there are wavelengths in recursive orders that are diffracted into the same direction. This results in spatial overlap of wavelengths satisfying $(n-1)\lambda_{n-1} = n\lambda_n$, which is obtained by the ratio of the grating equation for adjacent orders.

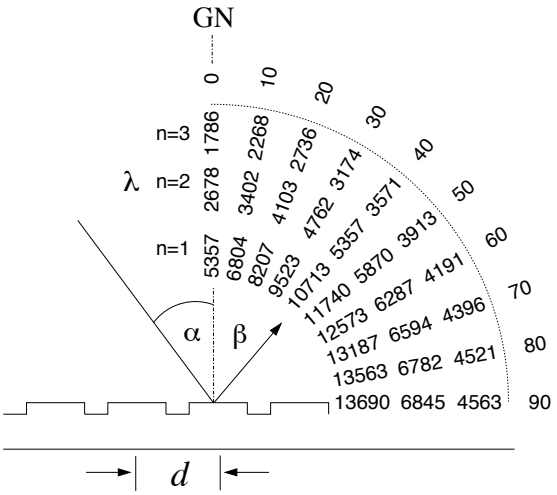

Figure 6.4: A schematic of the behavior of a grating with $1/d = 1200$ facets mm^{-1} for an incident angle $\alpha = 40°$. At each diffraction angle, β, the wavelengths for orders $n = 1$, 2, and 3 are tabulated, as governed by equation (Eq. 6.5). For $n = 0$, there is no dispersion and chromatic light beam is diffracted at $\beta = -\alpha$. Phase differences in the light reflection off adjacent facets interfere constructively for $\varphi_{cc} = n\pi$ for each λ, which yields monochromatic beams each diffracted at a unique β. Note that the dispersion increases with n according to Eq. 6.6.

The free spectral range for order n is defined as the wavelength range,

$$\Delta\lambda_n^+ = \lambda_{n-1} - \lambda_n, \tag{6.7}$$
$$\Delta\lambda_n^- = \lambda_n - \lambda_{n+1}, \tag{6.8}$$

for a given β. After substitution of the recursive relationship, $(n-1)\lambda_{n-1} = n\lambda_n$, we have

$$\Delta\lambda_n^+ = \lambda_n/(n-1), \tag{6.9}$$
$$\Delta\lambda_n^- = \lambda_n/(n+1). \tag{6.10}$$

Consider the free spectral range for the example grating illustrated in Figure 6.4 for $\beta = 40°$ at $n = 2$, which diffracts wavelength 5357 Å. We have $\Delta\lambda_2^+ = 5357/(2-1) = 5357$ Å, which yields 10713 Å for $\beta = 40°$ at $n = 1$, and $\Delta\lambda_2^- = 5357/(2+1) = 1786$ Å, which yields 3571 Å for $\beta = 40°$ at $n = 3$. Examination of Figure 6.4 illustrates this case.

The spatial overlap of different wavelengths can cause confusion in the recorded spectrum. There are two solutions to mitigate this confusion, depending upon whether the spectrograph is designed for low order or high order diffraction. In the case of small n, a blocking filter is placed in the light path (before the dispersion grating will work). For large n, a cross–dispersing grating is placed in the light path, after the dispersion grating. This latter approach is used for echelle spectrographs.

6.4.3 The interference function

In reality, there is a continuum of center–center interference phases that are periodic over continuous multiples of π. The generalized relationship between φ_{cc}, β, and each monochromatic diffracted λ is governed by

$$\varphi_{cc} = \frac{\pi d}{\lambda} (\sin\alpha + \sin\beta) . \tag{6.11}$$

Substituting $\varphi_{cc} = n\pi$ into Eq. 6.11, yields the grating equation (Eq. 6.5). The pattern of the normalized intensity for λ is called the interference function and is given by

$$\mathrm{I}_i(\varphi_{cc}) = \frac{\sin^2(L/d)\varphi_{cc}}{\sin^2\varphi_{cc}}, \tag{6.12}$$

where $L/d = N_f$, is an integer. For a given λ, there is a range of interference phases, which yield maximum intensity for $\varphi_{cc} = n\pi$ (constructive interference) and zero intensity for $\varphi_{cc} = (n/2)\pi$ (destructive interference).

In Figure 6.5*a*, the intensity function (Eq. 6.12) is plotted as a function of φ_{cc} for fixed λ. It is clear that the intensity pattern recorded for a given λ is not a δ–function, but is "smeared" over a small range of phase differences $\Delta\varphi_{cc} = \lambda/N_f d = \lambda/L$. The order separation of the peaks occurs when φ_{cc} is an integer multiple of λ/d.

Consider the example grating illustrated in Figure 6.4. For $\lambda = 5357$ Å in first order ($n = 1$), the diffraction angle is $\beta = 0°$, and for $n = 2$ is $\beta = 40°$. Naively, it would appear that one could place the camera at either location depending upon the desired dispersion (higher n location for higher disperion). However, as we will see below, the resulting intensity of the diffracted light is not equal for all orders for this type of grating due to additional phase differences introduced by the facet sizes, s.

6.4.4 The blaze function

As described by Eq. 6.12 and as illustrated in Figure 6.5*a*, the intensity pattern due to center–center diffraction is periodic and symmetric for all n. However, there is additional phase modulations that occur due to interference phases between the center and the edge of each facet. For center–edge interference, the relationship between β, λ, and the the center–edge phase φ_{ce} is

$$\varphi_{ce} = \frac{\pi s}{\lambda} (\sin\alpha + \sin\beta) . \tag{6.13}$$

The pattern of the normalized intensity for this inteference, called the blaze function, is given by

$$\mathrm{I}_b(\varphi_{ce}) = \frac{\sin^2\varphi_{ce}}{\varphi_{ce}^2}. \tag{6.14}$$

The blaze function is a maximum when $\varphi_{ce} = 0$, which occurs when the incident and diffraction angle are symmetric about the facet (grating) normal,

i.e., $\alpha = -\beta$. For plane–parallel (untilted) facets, as shown in Figure 6.4, this condition is met for $n = 0$ only. The minima occur at $\varphi_{ce} = n\pi$, so that the phase difference spread of the blaze function is $\Delta\varphi_{ce} = \lambda/s$. Note that this is a significantly broader width than that of the interference function, $\Delta\varphi_{cc} = \lambda/L$.

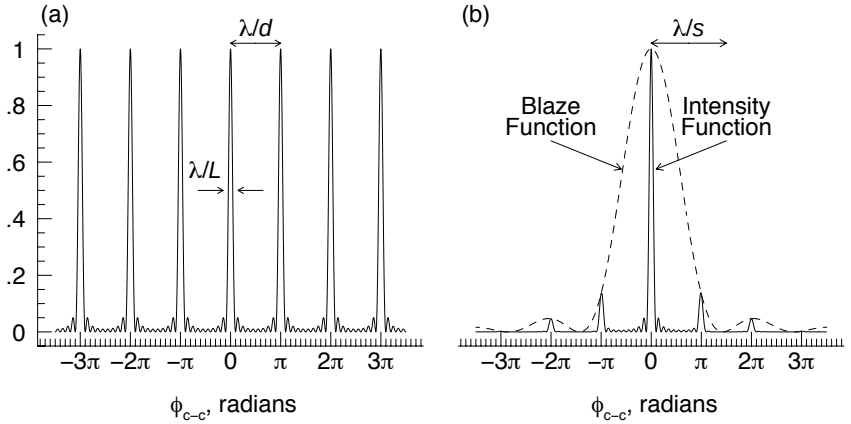

Figure 6.5: (*a*) The periodic interference function, Eq. 6.12, which results from the facet center–to–center interference, plotted as a function of the phase difference (in units of π) for an arbitrary wavelength λ. Note the peaks are at $n\pi$, where n is an integer. For this example, $N_f = L/d = 10$, which is an unrealisitc configuration used here only for illustration purposes. A typical grating might have $L = 40$ cm with 600 facets mm^{-1}, which gives $N_f = L/d = 24,000$; thus, real gratings have much narrower $\Delta\varphi_{cc}$ peaks. Note that each peak satisfies the grating equation (Eq. 6.5) and is thus diffracted at different β. (*b*) The blaze function, Eq. 6.14, which results from facet center–to–edge interference also plotted as a function of the phase difference of the center–center diffraction. The width of the blaze function is governed by the facet sizes; for this example the ratio $s/d = 0.7$ was used. The blaze function modulates the interference function, giving the overall intensity pattern, Eq. 6.16.

Naively, it might appear that φ_{ce} is a periodic function and that Eq. 6.14 would have multiple maxima, but this is not the case. The behavior of the blaze function for a given wavelenth at various orders is more clearly seen by solving the grating equation (Eq. 6.5) for λ and substituting into Eq. 6.13, which yields

$$\mathrm{I}_b(n) = \frac{\sin^2 n\pi(s/d)}{[n\pi(s/d)]^2}, \tag{6.15}$$

the relative blaze intensity for order n. It is because $d \neq s$ that φ_{ce}, and thus $\mathrm{I}_b(n)$, is not periodic. Note that $\mathrm{I}_b(n)$ peaks at $n = 0$ and decreases as n^2. The interpretation is that for a given λ appearing in multiple orders, the relative intensity is governed by Eq. 6.15.

It is not desirable to have the blaze function peak at $n = 0$, where there is no dispersion. The remedy is to "blaze" the grating by tilting the facets, which shifts the blaze peak. As we will show, it also yields blaze peaks for all values of n. This is discussed in § 6.4.6.

6.4.5 The intensity function

The resulting intensity function for light of wavelength λ, is the product of the interference and blaze functions,

$$\mathrm{I}(\lambda) = \mathrm{I}_i(\varphi_{cc}) \cdot \mathrm{I}_b(\varphi_{ce}) = \frac{\sin^2(L/d)\varphi_{cc}}{\sin^2 \varphi_{cc}} \cdot \frac{\sin^2 \varphi_{ce}}{\varphi_{ce}^2}. \tag{6.16}$$

As shown in Figure 6.5*b*, the resulting intensity pattern is simply the interference function modulated by the blaze function. Note that, for a non–blazed grating, the peak of the intensity occurs at $n = 0$, when $\alpha = -\beta$ (see Figure 6.4) and the inteference due to center–edge phase differences significantly reduces the throughput of light at higher orders. Again, this is more clearly seen by solving the grating equation (Eq. 6.5) for λ and substituting into Eq. 6.16, which yields the relative intensity for order n,

$$\mathrm{I}(n) = \mathrm{I}_i(n) \cdot \mathrm{I}_b(n) = \frac{\sin^2 n\pi(s/d)}{[n\pi(s/d)]^2}, \tag{6.17}$$

where $\mathrm{I}_i(n) = 1$ for all n. Thus, the relative intensity of a given wavelength at order n is modulated strictly by the blaze function.

Again, consider the example grating shown in Figure 6.4 for the ratio $s/d = 0.7$. To observe wavelength 5357 Å with the lowest dispersion ($n = 1$ and $\beta = 0°$) would be less than ideal because the intensity is modulated to roughly 10% its $n = 0$ throughput. Observing this wavelength at higher dispersion ($n = 2$ and $\beta = 40°$), would pose an even greater challenge because the intensity is modulated down even further. Note that 5357 Å does not appear in order $n = 3$ and above. By decreasing the ratio s/d, the blaze function can be broadened so that the throughput is increased for $n > 0$. However, this is not the most effective solution.

6.4.6 Blazing a grating

As shown above, the maximum efficiency in the intensity function occurs when the incident, α, and diffraction, β, angles are symmetric about the facet normal, which is the same as the grating normal, GN, when the grating facets are not tilted (as shown in the example grating in Figures 6.3 and 6.4).

From Eq. 6.6, we see that the dispersion, $d\beta/d\lambda$, scales as d/n, so in order to obtain a given resolving power for a spectrograph, it is desirable to maximize the intensity function (Eq. 6.16) for the required d and n combination. However, unless the blaze function is modified in some manner, the intensity pattern is maximized for $n = 0$ (no dispersion!) and is significantly reduced for large n.

In order to maximize the throughput at higher orders, the peak of the blaze function must be "shifted" along the φ_{cc} axis in Figure 6.5*b* such that it is centered at the desired n. By tilting the grating facets by an angle ϕ, as shown in Figure 6.6, the center–edge diffraction pattern can be phase shifted. In fact, blazing the grating has the added effect that the blaze function has a peak for

all n when the incident and diffraction angles are symmetric about the facet normal (which occurs for different λ for each n).

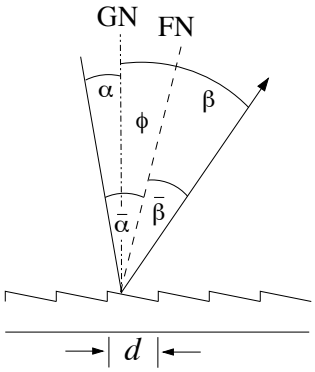

Figure 6.6: To maximize the diffraction illumination pattern for $n > 0$, a phase shift is introduced to the center–edge diffraction interference by grooving the facets at an angle ϕ, which also defines the facet nornal, FN. The blaze function then peaks when $\bar{\beta} = -\bar{\alpha}$.

The configuration for a blazed grating with facet tilts, ϕ, is illustrated in Figure 6.6. The facet lengths are now $s = d\cos^2\phi$, and the center–edge diffraction is based upon the angles with respect to the facet normal (FN, as is the case for the special case $\phi = 0°$). Defining the incident angle with respect to FN as $\bar{\alpha} = \alpha - \phi$ and the diffraction angle $\bar{\beta} = \beta - \phi$ (ϕ, α, and $\bar{\alpha}$ are defined positive, whereas β and $\bar{\beta}$ are negative), Eq. 6.13 is rewritten,

$$\varphi_{ce} = \frac{\pi s}{\lambda}\left[\sin\bar{\alpha} + \sin\bar{\beta}\right], \tag{6.18}$$

$$= \frac{\pi d\cos^2\phi}{\lambda}\left[\sin(\alpha-\phi) + \sin(\beta-\phi)\right]. \tag{6.19}$$

Recall that the blaze function (Eq. 6.14) is a maximum when $\varphi_{ce} = 0$. Thus, the optimal relationship between the facet tilts and the angles of incident and diffraction with respect to the grating normal, GN, is obtained when $\alpha - \phi = -(\beta - \phi)$, or $\phi = (\alpha + \beta)/2$. We will show that the blaze function for tilted facets peaks for all n at the λ dispersed into the $\bar{\beta} = -\bar{\alpha}$ direction, which occurs when the incident and diffraction angles are symmetric about the facet normal.

The wavelength at which the blaze function peaks at each order can be computed from the grating equation (Eq. 6.5). We have

$$\frac{n\lambda}{d} = \sin\alpha + \sin\beta, \tag{6.20}$$

$$= \sin(\bar{\alpha}+\phi) + \sin(\bar{\beta}+\phi). \tag{6.21}$$

Applying $\bar{\beta} = -\bar{\alpha}$, where the blaze function maximizes, yields,

$$\frac{n\lambda_b}{d} = 2\sin\phi\cos\bar{\alpha} = 2\sin\phi\cos(\alpha-\phi), \tag{6.22}$$

where λ_b is called the blaze wavelength for order n.

The general behavior of a blazed grating is more clearly seen by solving for d/λ_b in Eq. 6.22 and substituting into Eq. 6.18, which yields

$$\varphi_{ce} = \frac{n\pi \cos\phi[\sin\bar{\alpha} + \sin\bar{\beta}]}{2\tan\phi\cos\bar{\alpha}}, \tag{6.23}$$

where $s = d\cos^2\phi$ as been invoked. Clearly, the center–edge interference phase is $\varphi_{ce} = 0$ for $\bar{\beta} = -\bar{\alpha}$ diffraction for all n. As before, the relative intensity for order n is the interference function modulated by the blaze function at each $\bar{\beta}$,

$$\mathrm{I}(n,\bar{\beta}) = \mathrm{I}_i(n)\cdot\mathrm{I}_b(n,\bar{\beta}) = \frac{\sin^2\left(\dfrac{n\pi\cos\phi[\sin\bar{\alpha}+\sin\bar{\beta}]}{2\tan\phi\cos\bar{\alpha}}\right)}{\left(\dfrac{n\pi\cos\phi[\sin\bar{\alpha}+\sin\bar{\beta}]}{2\tan\phi\cos\bar{\alpha}}\right)^2} \tag{6.24}$$

where

$$\lambda(n,\bar{\beta}) = \frac{d}{n}\left(\sin\bar{\alpha} + \sin\bar{\beta}\right), \tag{6.25}$$

is the wavelength at each $\bar{\beta}$ at order n.

Equations 6.24 and 6.25 provide the basic relationships for spectrograph design. A central choice of the deisgn is, of course, the spectral dispersion (resolving power), which increases with increasing n/d. As such, the choice of n and d are critical. In the most general terms, spectrographs either work with lower dispersion in low orders, or in higher dispersions in higher orders. We discuss two example designs below.

6.5 Low order spectrographs

Low order gratings are generally blazed at $15^\circ \le \phi \le 20^\circ$ with $300 \le 1/d \le 1200$ facets mm^{-1} for orders $1 \le n \le 3$. It is desirable to have $\bar{\alpha} \sim \phi$. The blaze functions (Eq. 6.24) and solutions to the grating equation (Eq. 6.25) for a spectrograph with $\phi = 18^\circ$, $1/d = 600$ facets mm^{-1}, and $\bar{\alpha} = 22^\circ$ are illustrated in Figure 6.7 for orders $n = 1$, 2, and 3.

As can bee seen in Figure 6.7*a*, the blaze functions peak at $\bar{\beta} = -\bar{\alpha} = 22^\circ$ for all n. Note that the angular width of the blaze function scale as $1/n^2$. Only the range $0^\circ \le \bar{\beta} \le 90^\circ$ is presented. As seen in Figure 6.7*b*, the wavelengths of the blaze peaks scale with $1/n$.

This example spectrograph is configured for an optical wavelength range of 4000–8500 Å in order $n = 2$ for a camera centered at $\bar{\beta} = 22^\circ$ that subtends roughly 20° ($10^\circ \le \bar{\beta} \le 30^\circ$). Although many of these wavelengths appear in multiple orders, examination of Figures 6.7*c*–*e* reveals that they are diffracted toward different $\bar{\beta}$ for each n, which mitigates confusion. Consider the $n = 2$ blaze center, $\lambda \simeq 6500$ Å at $\bar{\beta} \simeq 22^\circ$. This wavelength is diffracted toward $\bar{\beta} \simeq 5^\circ$ for $n = 1$ and toward $\bar{\beta} = 55^\circ$ for $n = 3$. Both these diffraction angles reside will beyond the angular placement of the camera for $n = 2$.

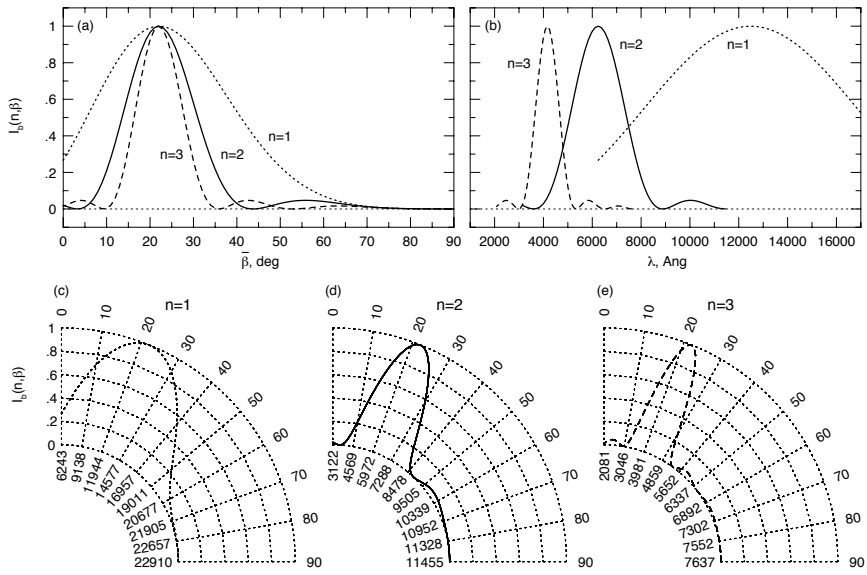

Figure 6.7: Solutions to Eqs. 6.24 and 6.25 for a spectrograph with at $\phi = 18°$, $1/d = 600$ facets mm^{-1}, and $\bar{\alpha} = 22°$, for orders $n = 1$, 2, and 3. (*a*) The dependence of the blaze functions on the diffraction angle, $\bar{\beta}$. (*b*) The blaze functions with wavelength, λ. (*c*, *d*, and *e*) The blaze functions shown in polar coordinate representation, which provides the spatial relationship between λ, $I_b(n, \bar{\beta})$, and $\bar{\beta}$.

Potential confusion can occur for $\lambda \leq 4860$ Å from $n = 3$ spatially overlapping with $\lambda \geq 4860$ Å from $n = 2$. In this case, a "high–pass" blocking filter that transmits $\lambda \geq 4860$ Å would eliminate the confusion. As such, this example spectrograph design is not optimal for blue wavelengths.

6.6 Echelle spectrographs

Echelle gratings can have a large range of ϕ, $\bar{\alpha}$, and d. However, some useful applications fall in the range of gratings blazed at $50° \leq \phi \leq 70°$ with $60 \leq 1/d \leq 80$ facets mm^{-1} for orders $20 \leq n \leq 100$. As with lower dispersion spectrographs, it is desirable to have the incident angle $\bar{\alpha} \sim \phi$. The blaze functions (Eq. 6.24) and solutions to the grating equation (Eq. 6.25) for an echelle spectrograph with $\phi = 52°$, $1/d = 70$ facets mm^{-1}, and $\bar{\alpha} = 70°$ are illustrated in Figure 6.8 for orders $n = 32$–70.

In Figure 6.8*a*, the blaze functions are shown as a function of wavelength. Orders 35, 45, 55, and 65 are labeled. In Figures 6.8*b*–*e*, the angular relationships for these four orders are illustrated. As with the low resolution design presented above, the widths of the blaze function become narrower as $1/n^2$. However, what is most striking is that each blaze function covers a narrow range of wavelengths (high dispersion) and is spatially aligned at $\bar{\beta} = -\bar{\alpha} = 70°$. For a camera and detector that are sensitive to the full optical and near–infrared

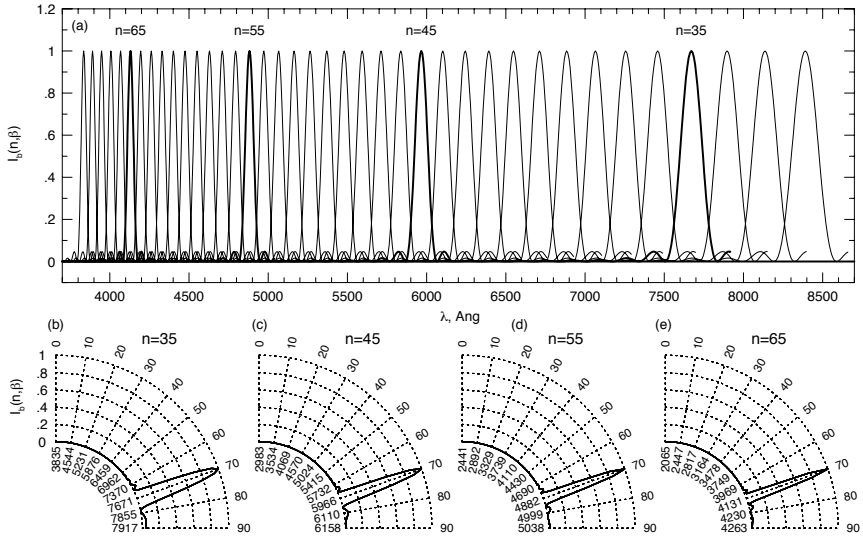

Figure 6.8: Solutions to Eqs. 6.24 and 6.25 for an echelle spectrograph with at $\phi = 52°$, $1/d = 80$ facets mm^{-1}, and $\bar{\alpha} = 70°$, for orders $n = 32$–70. (*a*) The blaze functions with wavelength, λ. (*b*, *c*, *d*, and *e*) The blaze functions shown in polar coordinate representation (for $n = 35$ 45, 55, and 65), which provide the angular relationship between λ, $I_b(n, \bar{\beta})$, and $\bar{\beta}$.

range (4000–9000 Å), there will be significant confusion due to the spatial overlap of the wavelengths present in each order. For example, all wavelengths at the blaze peaks shown in Figure 6.8*a* will overlap at $\bar{\beta} = 70°$.

To spatially separate the echelle orders, a second grating, called a cross disperser, is placed in the light path following the echelle grating. The cross disperser operates at low order, usually $m_x = 1$, and thus has grating parameters that are similar to the low order spectrograph example in § 6.5. The cross disperser is oriented such that the facets are at a right angle with respect to the echelle grating facets (on its side). Note that, if the cross disperser is a flat grating, the diverging light beam from the echelle grating must be recollimated, which can be accomplished with a refracting lens (though it is possible to use a concave grating for the cross disperser) to ensure an effective constant incident angle, α_x.

Consider a cross disperser grating with facet separations d_x blazed at ϕ_x operating in order m_x and oriented so that the post–echelle light is incident at angle α_x. The cross disperser will refract each wavelength into the direction β_x. Following the above convention, let $\bar{\alpha}_x = \alpha_x - \phi_x$ and $\bar{\beta}_x = \beta_x - \phi_x$ be the incident and refraction angles with respect to the cross disperser facet normals. The cross disperser introduces a two dimensional mapping of wavelength in the $\bar{\beta}_x$–$\bar{\beta}$ plane (using the convention that the echelle grating has no subscript).

The diffraction angle off the cross disperser is

$$\sin\bar{\beta}_{\rm x} = \frac{m_{\rm x}}{d_{\rm x}}\lambda(n,\bar{\beta}) - \sin\bar{\alpha}_{\rm x}, \tag{6.26}$$

where $\lambda(n,\bar{\beta})$ is taken from Eq. 6.25 for the echelle grating. From Eq. 6.6, the mapping will have a tilt in the $\bar{\beta}_{\rm x}$–$\bar{\beta}$ plane given by

$$\tan\Psi(\bar{\beta}_{\rm x},\bar{\beta}) = \frac{d\bar{\beta}_{\rm x}/d\lambda}{d\bar{\beta}/d\lambda} = \frac{m_{\rm x}}{d_{\rm x}}\frac{d}{n}\frac{\cos\bar{\beta}}{\cos\bar{\beta}_{\rm x}}. \tag{6.27}$$

The cross dispersion is relatively constant (though not strictly) for a given echelle order (small $\bar{\beta}_{\rm x}$ range) while the echelle dispersion is varying; as such the angle $\Psi(\bar{\beta}_{\rm x},\bar{\beta})$ will vary and the orders will have a slight curvature in the $\bar{\beta}_{\rm x}$–$\bar{\beta}$ plane. At the blaze peaks, the order separation will be

$$\sin\bar{\beta}_{\rm x} = 2\frac{m_{\rm x}}{m}\frac{d}{d_{\rm x}}\sin\bar{\alpha} - \sin\bar{\alpha}_{\rm x}, \tag{6.28}$$

which was obtained by subsituting $\bar{\beta} = -\bar{\alpha}$ into Eq. 6.25.

The overall echelle blaze function is then the blaze function of the echelle grating modulated by the blaze function of the cross disperser,

$$\mathrm{I}(m_{\rm x},\bar{\beta}_{\rm x},n,\bar{\beta}) = \mathrm{I}(n,\bar{\beta})\cdot\mathrm{I}(m_{\rm x},\bar{\beta}_{\rm x}) \tag{6.29}$$

where $\mathrm{I}(n,\bar{\beta})$ and $\mathrm{I}(m_{\rm x},\bar{\beta}_{\rm x})$ are the blaze functions for the echelle and cross disperser gratings obtained from Eq. 6.24.

The blaze functions (Eq. 6.24) and solutions to the grating equations (Eqs. 6.25 and 6.26) for a spectrograph with the above echelle grating parameters and a cross disperser with $\phi_{\rm x} = 14°$, $1/d_{\rm x} = 1200$ facets mm^{-1}, and $\bar{\alpha} = 22°$ are illustrated in Figure 6.9. Figure 6.9*a* illustrates the modulation of the echelle blaze functions by the cross disperser blaze function (dotted curve). As in Figure 6.8, orders $n = 35$, 45, 55, and 65 are shown as thick curves. Figure 6.9*b* illustrates the $\bar{\beta}_{\rm x}$ dependence of the cross disperser blaze function and its wavelength range in polar coordinates.

The mapping of wavelength in the $\bar{\beta}_{\rm x}$–$\bar{\beta}$ plane is illustrated in Figure 6.9*c*. The resulting mapping aligns the echelle orders in the $\bar{\beta}_{\rm x}$ direction with the order dispersion mapped in the $\bar{\beta}$ direction. Longer wavelength orders are diffracted to larger $\bar{\beta}_{\rm x}$, so that wavelength increases from the lower left to the upper right in the $\bar{\beta}_{\rm x}$–$\bar{\beta}$ plane. Order $n = 35$, with blaze wavelength $\lambda_b = 7671$ Å ($\bar{\beta} = 70°$) is centered at $\bar{\beta}_{\rm x} = 31°$, where as order $n = 55$, with blaze blaze wavelength $\lambda_b = 4882$ Å is centered at $\bar{\beta}_{\rm x} = 12°$. The free spectral range for each order is shown as the solid curves. Outside the free spectral range, a given wavelength is mapped in adjacent orders.

The main benefits of the echelle format is a large resolving power (high dispersion) with a large wavelength coverage while minimizing confusion; though it may be neccessary to use a blocking filter for the shorter wavelengths due to second order dispersion from the cross disperser. Clearly, a shortened slit

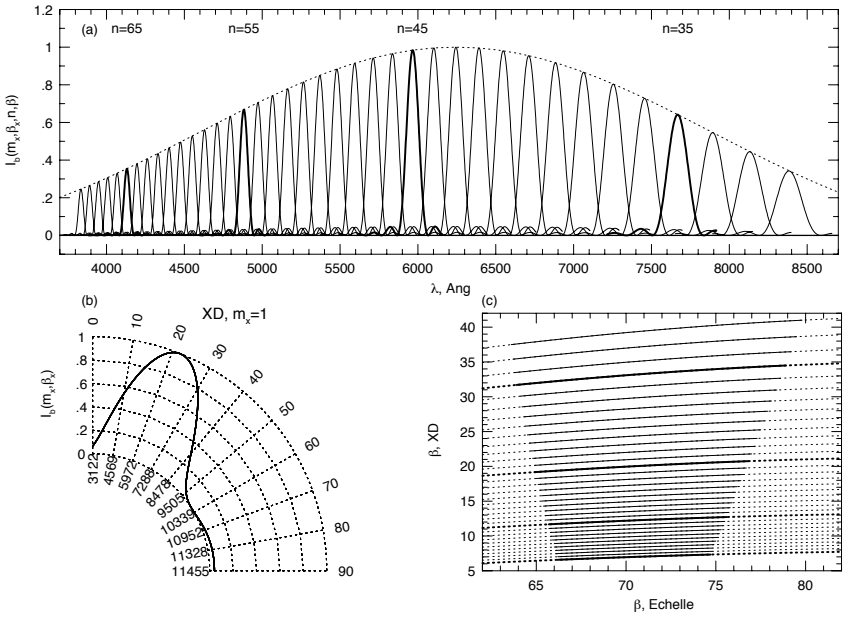

Figure 6.9: Solutions to Eqs. 6.24, 6.25, and 6.26 for the echelle grating illustrated in Figure 6.8 after being cross dispersed in order $m_{\rm x} = 1$ with a grating blazed at $\phi = 14°$, $1/d = 1200$ facets mm^{-1}, and $\bar{\alpha} = 22°$. (*a*) The dependence of the echelle blaze functions on wavelength, λ. The dotted curve is the cross disperser blaze function. (*b*) The cross disperser blaze function shown in polar coordinate representation, which provide the angular relationship between λ, $\mathrm{I}_b(m_{\rm x}, \bar{\beta}_{\rm x})$, and $\bar{\beta}_{\rm x}$. (*c*) The mapping of the echelle orders, n, in the $\bar{\beta}_{\rm x}$–$\bar{\beta}$ plane. Wavelength increases from the lower left to the upper right; orders $n = 35$ with $\lambda_b = 7671$ Å, $n = 45$ with $\lambda_b = 5966$ Å, $n = 55$ with $\lambda_b = 4882$ Å, and $n = 65$ with $\lambda_b = 4131$ Å are presented as thick curves. The solid curves provide the free spectral range of each order.

is required so that the sky does not overlap in the spatial (cross disperser) direction. If the orders are not well separated, a drawback of the echelle format is that background light from the sky may be difficult to sample. There can also be complications from scattered light from the many required optical elements.

6.7 Throughputs

In § 5.7, we discussed the attenuation of the observed flux due to the atmosphere, i.e., up to the point that the beam entered the telescope optics. We called this flux the "attenuated flux", $F_\lambda^{\rm A} = \epsilon_\lambda^{\rm A}(z) F_\lambda$. As the attenuated flux passes through the telescope optics and spectrograph elements, i.e., the slit, collimator, grating and camera, further attenuations occur. The product of all these attenuation factors (excluding the atmosphere) is known as the throughput of the telescope plus spectrograph facility. In practice, the throughput is the ratio of the flux impinging upon the detector to the flux entering the telescope (i.e., the attenuated flux).

6.7.1 Telescope

As the beam passes through the telescope, reflections off the primary and secondary (and possible tertiary) mirrors and transmissions through possible refractive focusing elements result in a series of wavelength dependent attenuations. These attenuations occur prior to the light reaching the spectrograph instrument itself. Thus, the spectrum reaching the slit aperture of the spectrograph is further modified by the transmission factor $\epsilon_\lambda^{\rm T}$, which is the ratio of the flux entering the spectrograph to the flux entering the telescope. The form $\epsilon_\lambda^{\rm T}$ is usually smooth and well behaved.

6.7.2 Slit loss

For a point source, if the slit width is narrower than the seeing disk, then some light will not be passed into the spectrograph. This light loss at the slit, commonly referred to as "slit losses" can be significant (Filippenko, 1982). If the surface brightness profile of the seeing disk is given by Eq. 6.1, and the slit width and height are w and h, respectively, then the fraction of seeing disk that passes through the slit is

$$\begin{aligned}\epsilon_\lambda^{\rm S} &= \frac{1}{2\pi\,\sigma_\lambda^2}\int_{-w/2}^{w/2}\int_{-h/2}^{h/2}\exp\left\{-\frac{u^2+v^2}{2\sigma_\lambda^2}\right\}dudv \\ &= W(w/2,\sigma_\lambda)\,H(h/2,\sigma_\lambda)\,,\end{aligned} \tag{6.30}$$

where

$$\begin{aligned}W(w/2,\sigma_\lambda) &= \frac{1}{\sqrt{2\pi}\,\sigma_\lambda}\int_{-w/2}^{w/2}\exp\left\{-\frac{u^2}{2\sigma_\lambda^2}\right\}du \\ H(h/2,\sigma_\lambda) &= \frac{1}{\sqrt{2\pi}\,\sigma_\lambda}\int_{-h/2}^{h/2}\exp\left\{-\frac{v^2}{2\sigma_\lambda^2}\right\}dv\,,\end{aligned} \tag{6.31}$$

where $r^2 = u^2 + v^2$, with u and v representing the physical coordinates in the telescope focal plane parallel to w and h respectively,

Via the plate scale (Eq. 6.2), Eq. 6.30 is directly expressable in units of [arcsec]. Consider a scenario in which the seeing is $\theta_{\sigma_\lambda} = 0.9$ [arcsec], which corresponds to $\sigma_\lambda = 0.38$ [arcsec]. For a long–slit configuration, $h \gg \sigma_\lambda$ and $H(h/2,\sigma_\lambda) = 1$. If the slit width is $w = 1$ [arcsec], then we find that $\epsilon_\lambda^{\rm S} = 0.811$. This result holds in general for a long slit observation in which $w/\theta_{\sigma_\lambda} = 1.1$.

The situation is aggravated if the seeing disk is not well centered replacing x in Eq. **??** with $x - u_0$. However, it is mathecatically equivalent to transpose the limits of integration if the seeing disk is divided at its center point in the focal plane, giving

$$\epsilon_\lambda^{\rm S} = \left[\frac{W(w/2-u_0,\sigma_\lambda) + W(w/2+u_0,\sigma_\lambda)}{2}\right] H(h/2,\sigma_\lambda)\,, \tag{6.32}$$

In practice, the angle of the slit projected on sky governs the wavelength behavior of slit losses because of the wavelength dependent refraction of the beam through the atmosphere. We disuss atmospheric dispersion effects at the slit in § **??**.

6.7.3 Collimator and grating

The second optical element in the spectrograph is the collimator. The reflective properties of the collimator can be characterized by a transimission efficiency factor, $\epsilon_\lambda^{\rm C}$. However, the dominant modification of the flux with wavelength comes from the blaze function of the grating. We write the transmitted efficiency factor of the grating as

$$\epsilon_\lambda^{\rm G} = \varepsilon_\lambda^{\rm G} {\rm I}(\lambda), \tag{6.33}$$

where $\varepsilon_\lambda^{\rm G}$ is the reflectivity efficiency of the grating and $\rm I(\lambda)$ is the intensity function (product of interference and blaze functions) given by Eq. 6.24 for a low order spectrograph and Eq. 6.29 for an echelle spectrograph, and where λ is given by Eq. 6.25. Examples of the wavelength functional form of $\epsilon_\lambda^{\rm G}$ are illustrated in Figure 6.7*b* for low order and in Figure 6.9*a* for echelle spectrographs. The highly variable form of $\epsilon_\lambda^{\rm G}$ results in a significant modification to the flux.

6.7.4 The modified flux

We defer discussion of the camera throughput until § 6.11, following discussion of the spectral purity. For the light path followed so far, we have the modified flux post grating reaching the spectrograph camera optics

$$F_\lambda^{\rm G} = \epsilon_\lambda^{\rm G}\, \epsilon_\lambda^{\rm C}\, \epsilon_\lambda^{\rm S}\, \epsilon_\lambda^{\rm T}\, F_\lambda^{\rm A}. = \epsilon_\lambda^{\rm G}\, \epsilon_\lambda^{\rm C}\, \epsilon_\lambda^{\rm S}\, \epsilon_\lambda^{\rm T}\, \left[\epsilon_\lambda^{\rm A}\, F_\lambda\right] . \tag{6.34}$$

The overall wavelength dependence of this modified flux will no longer closely resemble the overall wavelength behavior of the attenuated flux nor the observed flux (that incident upon the upper atmosphere). In fact, the modified flux reaching the camera will strongly reflect the form of $\epsilon_\lambda^{\rm G}$ due to the highly variable blaze function of the spectrograph grating (or gratings in the case of echelle spectrographs).

6.8 Resolving power of the grating

The monochromatic resolving power of the grating is obtained from the grating equation (Eq. 6.5),

$$\varphi_{cc}(n) = \frac{n\lambda}{d} = \sin\alpha + \sin\beta, \tag{6.35}$$

where $\varphi_{cc}(n\pi)$ is defined as the center–to–center phase difference from reflection off of adjacent facets for integer multiples of π. As we showed in § 6.4.5, from

the intensity function (Eq. 6.16) illustrated in Figure 6.5*a*, the width of the interference maxima is given by

$$\Delta\varphi_{cc}(n) = \frac{\lambda}{L}, \tag{6.36}$$

which also follows from the standard theorem of Fourier transforms that data sampled with a window Δ have frequency widths of $1/\Delta$; in this case the length of the grating, L, (this is the same principle by which the diffraction limited resolving power of a telescope is λ/D, where D is the telescope diameter). Differencing the grating equation yields

$$\Delta\varphi_{cc}(n) = \frac{n}{d}\Delta\lambda_{\rm G}. \tag{6.37}$$

Equating Eqs. 6.36 and 6.37 gives

$$\Delta\lambda_{\rm G} = \frac{\lambda}{n}\frac{d}{L}. \tag{6.38}$$

The definition of the grating monochromatic resolving power, $R_{\rm G}$, is

$$R_{\rm G} = \frac{\lambda}{\Delta\lambda_{\rm G}} = n\frac{L}{d}, \tag{6.39}$$

which is a constant with wavelength for a given spectral order, and grating configuration, depending only upon the ratio of the facet length to the grating length (equals the number of facets, N_f).

6.9 Spectrograph resolving power

In practice, the resolvng power, or resolution, of a spectrograph, R, is lower than the monochromatic resolution of the grating, $R_{\rm G}$. The spectral resolution is dominated by the so–called spectral purity, which is a measure of the width of a monochromatic image of the slit.

Consider a monochromatic light source with an image that fills the slit as seen from the collimator. Light from one edge of the slit strikes the collimator, and therefore the grating, with a slightly different incident angle, α, than light from the other edge of the slit. If the slit width is w, then the angular size at the collimator, and therefore the range of incident angles on the grating is

$$d\alpha = \frac{w}{f_{coll}}. \tag{6.40}$$

The spectral purity is the spatial broadening of the monochromatic image of the slit at the detector (camera focal plane). That is, it is the linear dispersion in wavelength at the detector for a chromatic wavefront due to the small range of reflection angles off the grating. The range of reflection angles, $d\beta$, off the

grating are due to the range of incident angles, $d\alpha$, due to the finite slit width, w. The relationship between $d\alpha$ and $d\beta$ follows from the grating equation, Eq. 6.5,

$$\frac{n}{d}d\lambda = \cos\alpha\, d\alpha + \cos\beta\, d\beta, \tag{6.41}$$

which, for a monochromatic source, i.e., $d\lambda = 0$, gives

$$d\beta = -\frac{\cos\alpha}{\cos\beta}\, d\alpha. \tag{6.42}$$

In physical coordinates, x, the size of the image of the slit at the detector focal plane is given by the relation

$$dx = f_{cam} d\beta, \tag{6.43}$$

which gives the physical extent the image of the slit, w',

$$w' = f_{cam}\, d\beta = -f_{cam}\frac{\cos\alpha}{\cos\beta}\, d\alpha = -w\frac{f_{cam}}{f_{coll}}\frac{\cos\alpha}{\cos\beta}, \tag{6.44}$$

where Eqs. 6.42 and 6.40 have been substituted for $d\beta$ and $d\alpha$, respectively. The ratio w'/w is the magnification in the dispersion direction (the ratio f_{cam}/f_{coll} is the magnification in the spatial, or cross–dispersion, direction). Note that the image is inverted (as indicated by the negative sign).

The conversion of the physical coordinates, x, of the slit image on the focal plane (detector) into dispersion coordinates, λ, is given by

$$\Delta\lambda = w'\frac{d\lambda}{dx} = w'\frac{d\lambda}{d\beta}\frac{d\beta}{dx} = \frac{w'}{f_{cam}}\frac{d\lambda}{d\beta}, \tag{6.45}$$

where Eq. 6.43 has been substituted for $d\beta/dx$. From Eq. 6.41, we have the angular dispersion

$$\frac{d\lambda}{d\beta} = \frac{d}{n}\cos\beta, \tag{6.46}$$

which, after substitution into Eq. 6.45, and substituting Eq. 6.44 for w', gives the spectral purity

$$\Delta\lambda = -\frac{w}{f_{coll}}\frac{d}{n}\cos\alpha. \tag{6.47}$$

What Eq. 6.47 tells us is that if we represent the distribution of incident monochromatic light as a unit–area delta function at wavelength λ, i.e., δ_λ, then the resulting intensity pattern will be dispersed over a range of wavelength for which the full–width half–maximum will be $\Delta\lambda$. This clearly represents a degradation of the purity of the incoming spectrum.

Smaller $\Delta\lambda$ may be desired, but there are practical trade offs. It is clear that one would like to work with α approaching $\pi/2$ at high orders. These two consideration requires a larger facet angle, ϕ. Also, smaller facet spacings, d, are desirable. A narrower slit width decreases $\Delta\lambda$, but the trade off is that if the width is narrower than the atmospheric seeing (assuming a point source), there

is light loss at the slit. A long collimator focal length is often a viable solution, but this will require a long light path and a large collimator and grating size.

The actual limiting resolution of the spectrograph is then obtained from the ratio of the grating equation (Eq. 6.5) to the spectral purity (Eq. 6.47), giving the general expression,

$$R = \frac{\lambda}{\Delta\lambda} = \frac{f_{coll}}{w}\frac{n^2}{d^2}\left(\frac{\sin\alpha + \sin\beta}{\cos\alpha}\right). \tag{6.48}$$

Note that the spectrograph resolution is maximized for a narrow slit and a long collimator focal length. It is important, however, to consider the physical pixel size on the detector. It is a poor design to under sample or oversample $\Delta\lambda$. The former yields a loss of information, and the latter must be paid for by longer observations. We touch on these issues below.

6.10 Instrumental spread function

§ **??**.

As discussed in §§ 6.8 and 6.9, the amount of dispersion of the light is characterized by the resolution

$$R = \frac{\lambda}{\Delta\lambda}, \tag{6.49}$$

where $\Delta\lambda$ is the spectral purity given by Eq. 6.47, which describes the "blurring" of monochromatic beams on the detector.

In practice, the *distribution* of this blurring can be a complex function, called the instrumental spread function (ISF), denoted $\Phi_\lambda(\Delta\lambda)$. The spectral purity, $\Delta\lambda$, quantifies the full–width half–maximum (FWHM), of the ISF, which has unit area

$$\int_0^\infty \Phi_\lambda(\Delta\lambda)\, d\lambda = 1. \tag{6.50}$$

The ISF is often measured and published by the spectrograph commissioning team.

For a well–behaved spectrograph, the ISF can be approximated as a normalized, symmetric Gaussian function,

$$\Phi_\lambda(\Delta\lambda) = \Phi_\lambda(\lambda' - \lambda) = \frac{1}{\sqrt{2\pi}\Delta\sigma}\exp\left[-\frac{(\lambda'-\lambda)^2}{2(\Delta\sigma)^2}\right], \tag{6.51}$$

where $\Delta\sigma = \Delta\lambda/2.35$, and where $\Delta\lambda$ is the FWHM of a monochromatic light beam. A monochromatic beam described by a unit–area delta function, δ_λ, will be dispersed so that the intensity pattern is redistributed with wavelength according to the ISF (for example, following Eq. 6.51 if a Gaussian distribution is assumed). Since the incident spectrum can be viewed as a continuous series of adjacent δ_λ functions, the consequence of Eq. 6.51 is that measured flux at wavelength λ will include contributions of flux from incident wavelength λ' in proportion to $\Phi_\lambda(\Delta\lambda)$.

6.10.1 The resolution element

The spectral purity, $\Delta\lambda$, as given by Eq. 6.47, is often called the *resolution element* (again, defined as the FWHM of the ISF). Very narrow absorption lines, those with widths much narrower than $\Delta\lambda$, will have the shape of $\Phi_\lambda(\Delta\lambda)$ with FWHM $= \Delta\lambda$. Such features are called *unresolved lines*. As such, if one measures the FWHM of an absorption line and it is consistent with resolution element, $\Delta\lambda$, then the line is considered to be unresolved. If the measured FWHM is substantially broader than the resolution element, then the line is considered to be a *resolved line*. The distinction is not so clear when the measured FWHM of the line is slightly broader than the resolution element, though the terms "partially resolved" and "moderately resolved" apply.

Note that the FWHM of an unresolved line is dependent upon the observed wavelength in the spectrum. Because the resolution, R, is a constant, the observed widths of unresolved lines get broader in direct proportion to wavelength, i.e., $\Delta\lambda \propto \lambda$ (see Eq. 6.48).

6.11 The apparent flux

Consider the flux entering the spectrograph. The beam first passes through the slit, suffering slit loss $\epsilon_\lambda^{\rm S}$, and then reflects off the collimator, which modifies the flux by the factor $\epsilon_\lambda^{\rm C}$. Following dispersion and reflection off the grating, the flux is *simultaneously* modified by the grating blaze function (over large wavelength ranges) and has its spectral purity degraded over small wavelength ranges on the order of $\Delta\lambda$. The beam then passes through the camera optics with transmission factor $\epsilon_\lambda^{\rm O}$.

Thus, the "apparent flux" incident upon the detector is then

$$F_\lambda^{(a)} = \epsilon_\lambda^{\rm O}\left\{\Phi_\lambda(\Delta\lambda) \otimes [F_\lambda^{\rm G}]\right\}, = \epsilon_\lambda^{\rm O}\left\{\Phi_\lambda(\Delta\lambda) \otimes [\epsilon_\lambda^{\rm G}\,\epsilon_\lambda^{\rm C}\,\epsilon_\lambda^{\rm S}\,\epsilon_\lambda^{\rm T}\,\epsilon_\lambda^{\rm A}\,F_\lambda]\right\}, \qquad (6.52)$$

accounting for attenuation from the atomsphere (A) and telescope (T), slit losses (T), and reflectivity off the collimator (C), reflectivity and disperiosn off the grating (G), degredation of the spectral purity [convolution with the ISF, $\Phi_\lambda(\Delta\lambda)$], and transmission through the camera (O). Note that the apparent flux is written as a series of mathematical operations (from right to left) acting on the observed flux in the same order as the processes act on the light beam as it propagates through the spectrograph.

The term "apparent flux" (the origin of the term will be discussed further below) is applied because of the degredation of the spectral purity, which results in a redistribution of the flux values. It is this apparent flux that is to be captured by the detector. The convolution of the ISF in Eq. 6.52 is critically important in spectral regions where the flux level changes rapidly on wavelength intervals comparable to the resolution element, $\Delta\lambda$ (such as in the wing of an absorption line or across the profile of an unresolved absorption line). Where the flux level varies slowly, such as in the continuum of the spectrum, the convolution to account for the degredation of the spectral purity has negligble effect on the

flux level, so that

$$F_\lambda^{(c)} = \epsilon_\lambda^{\rm O}\epsilon_\lambda^{\rm G}\,\epsilon_\lambda^{\rm C}\,\epsilon_\lambda^{\rm S}\,\epsilon_\lambda^{\rm T}\,\epsilon_\lambda^{\rm A}\,F_\lambda^0, \tag{6.53}$$

where the superscript "c" indicates continuum flux.

6.11.1 Apparent optical depth

The term apparent flux derives from the concept of the apparent optical depth. Consider an absorption feature with optical depth τ_λ, such that

$$F_\lambda = F_\lambda^0 \exp\{-\tau_\lambda\}, \tag{6.54}$$

where F_λ is the observed flux and F_λ^0 is the observed continuum flux. Writing the convolution in Eq. 6.52 explicitly, we have

$$F_\lambda^{(a)} = \epsilon_\lambda^{\rm O}\int_{\lambda_-}^{\lambda_+}\Phi_\lambda(\lambda'-\lambda)\,\epsilon_{\lambda'}^{\rm G}\,\epsilon_{\lambda'}^{\rm C}\,\epsilon_{\lambda'}^{\rm S}\,\epsilon_{\lambda'}^{\rm T}\,\epsilon_{\lambda'}^{\rm A}\,F_{\lambda'}^0\exp\{-\tau_{\lambda'}\}\,d\lambda', \tag{6.55}$$

where the limits of integration, λ_- and λ_+, are taken to be large enough to bracket the absorption feature or span several resolution elements. It is required that this integral is evaluated at each λ (over the range $\lambda_- \le \lambda' \le \lambda_+$) to obtain $F_\lambda^{(a)}$ at each wavelength. That is, the full apparent flux spectrum is obtained by evaluating the integral at each λ. In the continuum, i.e., regions of the spectrum where the flux values varies smoothly over wavelength scales much greater than $\Delta\lambda$ (the resolution element), the continuum flux incident on the detector can be well approximated by Eq. 6.53.

Since the convolution of the ISF degrades the spectrum, effectively redistributing the flux within the absorption line profile, one cannot simply determine the true optical depth. The true optical depth is reflected accurately in the observed flux (prior to attenuation through the atmosphere),

$$\tau_\lambda = -\ln\left[\frac{F_\lambda}{F_\lambda^0}\right]. \tag{6.56}$$

However, only the apparent flux is measured following attentuation through the atmosphere and telescope optics, and then through the spectrograph, including degredation of the spectral purity. Thus, only the apparent optical depth can be deduced via inversion of the spectrum of the apparent flux

$$\tau_\lambda^{(a)} = -\ln\left[\frac{F_\lambda^{(a)}}{F_\lambda^c}\right]. \tag{6.57}$$

The continuum flux over the wavelength region of the absorption profile would need to be determined by interpolating F_λ^c across the profile using adjacent wavelength regions of the spectrum. We will discuss the interpolation and the application of the apparent optical depth in later chapters.

6.11.2 Convolution of the ISF

In Figure 6.10*a*, the relative observed flux, $F_\lambda = \exp\{-\tau_\lambda\}$, of a set of typical Ly$\alpha$ absorption lines ($\lambda_r = 1215$ Å) is convolved with Gaussian representations of the ISF for five typical spectral resolutions, $R = 450$, 2250, 4500, 9000, and 20,000, which are illustrated in Figure 6.10*b*. The resolution element of the ISF (FWHM) is $\Delta\lambda = \lambda/R$. The normalized apparent flux absorption profiles, $F_\lambda^{(a)} = \exp\{-\tau_\lambda^{(a)}\}$, are presented in Figure 6.10*c* for each resolution. All panels are given in relative wavelength units centered at λ_r.

Note that the $R = 450$ panels cover a broader relative wavelength scale. Vertical dot–dot lines provide a guide for the eye to the location of the wavelength extent of the intrinsic profile. In this example, the intrinsic line widths are very narrow, and this results in an almost complete "washing out" of the absorption line in the $R = 450$ case. As resolution increases, the shape of the apparent flux profile approaches the shape of the intrinsic profile.

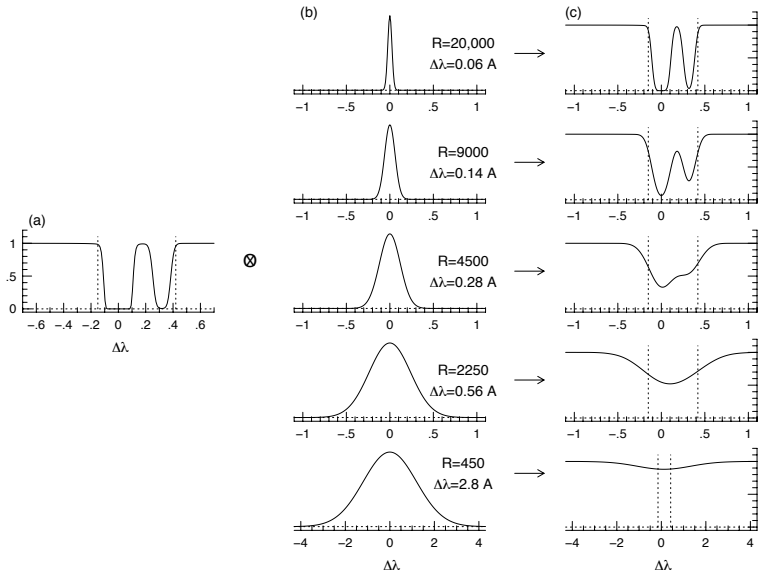

Figure 6.10: Illustrations of the reduction in spectral purity via convolution of the ISF for five somewhat typical spectroscopic resolutions, $R = 450$, 2250, 4500, 9000, and 20,000 (increasing from the lower to the upper panels). (*a*) The observed flux illustrating the intrinsic Lyα profile entering the spectrograph in relative wavelength units, centered at 1215 Å. (*b*) The Gaussian ISF profiles for the five resolutions, with $\Delta\lambda$ (FWHM) labeled for each. Note the different scale of each panel. (*c*) The apparent flux profiles for each resolution over the same relative wavelength scales. Vertical lines at $\Delta\lambda = -0.15$ and 0.42 provide wavelength range of the intrinsic profile.

From this example, it becomes quite clear that only the apparent optical depth can be determined from the measured apparent flux, given how dramatically the apparent flux differs from the observed flux. Low resolution can result in non–detections (once noise and pixelization sampling are accounted for). Note the slight offset of the profile center in the $R = 2250$ case. Though the double

nature of the line profile begins to appear at $R = 4500$, it is not until $R = 9000$ that the apparent flux profile takes on a shape approaching the observed flux profile.

It is also important to realize that even for a saturated profile, where the counts are zero in the core of the observed flux profile, the apparent flux in such a profile may not reach zero, depending upon the resolution. Note also the level of recovery of the apparent flux in the continuum between the two features is highly dependent upon resolution. Not until $R = 20,000$ is there any real hope of measuring or confidently constraining the properties of the absorption lines.

6.12 Pixelization

The charged couple device (CCD) is the commonly favored detector for astronomical spectrographs. A CCD is effectively a two–dimensional array of independent semi–conductors, known as pixels. The final step of the light beam is to be collected in these discrete pixels. The process of pixelization is mathematically equivalent to multiplying the apparent flux with an infinite series of box functions

$$B(x)\, III(x) = B(x) \left[\sum_{k=0} \delta \left(x - k \frac{B(x)}{2} \right) \right], \quad k = \text{integer}, \tag{6.58}$$

where x is the physical coordinate on the CCD increasing in steps of k in the dispersion direction of the incident spectrum, and where $B(x)$ is the width of the pixels centered about the centroid of each of the $III(x)$, known as the Shaw function. Thus, the physical positions and extent of the pixels are represented by the function $B(x)\, III(x)$. Note that this function is fixed by design of the detector. Typically, pixels have $B(x)$ on the order of 20 [microns pixel^{-1}].

6.12.1 Pixel plate scale

The pixel plate scale is the angular projection on the sky imaged by each pixel on the CCD. It is usually express in [arcsec pixel^{-1}]. The pixel plate scale is the product of the physical pixel width, the plate scale at the telescope focal plane, and the magnification factor of the telescope image at the slit due to the spectrograph optics and diseprsion properties.

As introduced in § 6.3, $\theta_{\rm ps} = 1/f_{\rm T}$ is the plate scale in the telescope image plane (at the slit), where $f_{\rm T}$ is the effective focal length of the telescope. From Eq. 6.44, we have the magnification, w'/w, in the dispersion direction in the focal plane of the spectrogaph, i.e., at the detector along the x coordinate (also see Figure 6.2). The plate scale in the x direction is therefore $\theta_x = \theta_{\rm ps}(w'/w)$,

$$\theta_x = \frac{1}{f_{\rm T}} \frac{f_{cam}}{f_{coll}} \frac{\cos\beta}{\cos\alpha}, \tag{6.59}$$

in [radians cm^{-1}] if $f_{\rm T}$ is given in [cm]. Similarly, the plate scale in the spatial direction y is $\theta_y = \theta_{\rm ps}(h'/h)$,

$$\theta_y = \frac{1}{f_{\rm T}} \frac{f_{cam}}{f_{coll}}, \tag{6.60}$$

also in [radians cm^{-1}].

To convert the plate scales into [arcsec pixel^{-1}], we multiply by $B(x)$ for the dispersion direction and $B(y)$ for the spatial direction and convert units. Pixels are usually square, so that $B(y) = B(x)$. The pixel plate scale, PS, is then,

$$\mathrm{PS}_x = C\, B(x)\, \theta_x = C\, \frac{B(x)}{f_{\rm T}} \frac{f_{cam}}{f_{coll}} \frac{\cos\beta}{\cos\alpha}\,, \tag{6.61}$$

$$\mathrm{PS}_y = C\, B(y)\, \theta_x = C\, \frac{B(y)}{f_{\rm T}} \frac{f_{cam}}{f_{coll}}\,, \tag{6.62}$$

where $B(x)$ and $B(y)$ are in [microns pixel^{-1}], and the focal lengths are in [cm], giving

$$C = 206,265 \cdot \left[\frac{1\ \mathrm{m}}{10^9\ \mu\mathrm{m}}\right] \left[\frac{10^2\ \mathrm{cm}}{1\ \mathrm{m}}\right] = 2.06266 \times 10^{-2}\,, \tag{6.63}$$

where the constant 206,265 is the number of [arcsec radian^{-1}], and C is in [arcsec cm micron^{-1}].

A well designed telescope/spectrograph facility will have a pixel plate scale on the order of 1/3 or less of the best seeing disk of a point source. The extent of a typical seeing disk depends upon the accuracy of the guiding and the typical atmospheric seeing conditions. If the best conditions, for example, provide a seeing disk of 0.6 [arcsec], then a pixel scale of $\mathrm{PS}_y = 0.2$ [arcsec pixel^{-1}] would be a maximum acceptable value (sampling three pixels across the FWHM of the seeing disk in the spatial direction). A pixel plate scale somewhat smaller than $\simeq 0.1$ [arcsec pixel^{-1}] is typical for ground–based facilities. CCD pixels can be binned. When binning, the plate scale must be corrected by the number of pixels per binned pixel.

6.12.2 Dispersion per pixel

The spectrograph camera focuses the collimated dispersed beam such that each pixel independently collects incident apparent flux at λ over the range $\Delta\lambda_{\rm pix}$. How the physical pixel widths, $B(x) = \Delta x_{\rm pix}$, translate to wavelength intervals depends upon the spectrograph design, according to Eqs. 6.43 and 6.46, giving

$$\frac{\Delta\lambda_{\rm pix}}{\Delta x_{\rm pix}} = \frac{d\lambda}{dx} = \frac{d}{n} \frac{\cos\beta}{f_{cam}}. \tag{6.64}$$

Since β is λ dependent via the grating equation (Eq. 6.5), the λ coordinate will not map linearly with x nor will the wavelength interval of each pixel, $\Delta\lambda_{\rm pix}$. Having mapped the wavelength dispersion to the physical location of the pixels, the pixels can now be mapped according to $B(x)\, III(x) \mapsto B_\lambda\, III_\lambda$, which have magnitude $B_\lambda = \Delta\lambda_{\rm pix}$ [Å pixel^{-1}].

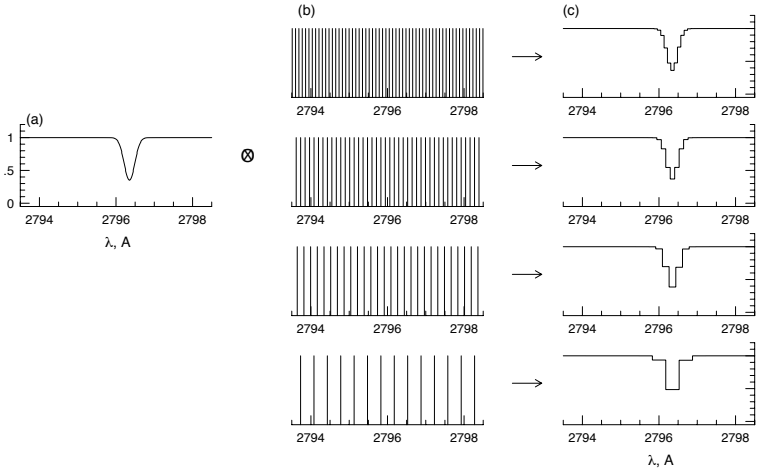

Figure 6.11: Examples of pixelization for an $R = 8000$ unresolved absorption line at $\lambda = 2796.35$ (panel a) for four different sampling rates. (b) The Shah function, Eq. 6.58, for sampling rates corresponding to $p = 1$, 2, 3, and 4. $\Delta\lambda_{\rm pix} = p\Delta\lambda$, where $\Delta\lambda = \lambda/R$ is the resolution element. (c) The sampled spectra for each p.

6.12.3 Pixels per resolution element

The sampling rate of the spectrum is described by the number of pixels per resolution element, $\Delta\lambda = \lambda/R$, defined as

$$p = \frac{\Delta\lambda}{\Delta\lambda_{\rm pix}} = \frac{\lambda/R}{\Delta\lambda_{\rm pix}}, \tag{6.65}$$

where $\Delta\lambda_{\rm pix}$ is the wavelength extent of a single pixel at λ. In Figure 6.11, the pixelization of an unresolved absorption line with $R = 8000$ at $\lambda = 2796.35$ is illustrated for four integer values of p (though it is not required that p is an integer). The relative apparent flux of the line profile prior ro pixelization is illustrated in Figure 6.11a. In Figure 6.11b, the function $B_\lambda\, III_\lambda$ is presented for $p = 1$, 2, 3, and 4 (lower to upper). In Figure 6.11c, the resulting sampled profile is shown for each p. The Shah function has been centered on the absorption line; for $p \leq 2$, the shape of the pixelized absorption line is sensitive to where the line centroid falls with respect to the center of $B_\lambda\, III_\lambda$.

A pixel sampling rate of $p = 2$ is known as being "critically sampled". In otherwords, it represents the smallest sampling rate in which any integrity can be preserved in sampling the instrumental spread function for the spectrograph (for $p = 2$, two pixels record the FHWM of the ISF). These considerations follow from the theorem describing the Nyquist sampling frequency, below which aliasing of the original input signal occurs.

6.13 Count flux and total counts

The recording of the apparent flux focused into a given pixel on the CCD consists of counting the *number* of incoming photons that have impinged upon the pixel over some fixed time interval. Thus, we must know the number flux of photons impinging upon a given pixel. To obtain the total number of photons, we then multiply the number flux by the time interval that photons were collected and the collecting area of the telescope facility.

Photons are counted by storing and then counting the number of electrons liberated by the incoming photons in the semi–conducting material. The efficiency of this process is not perfect and is wavelength dependent; it is known as the quantum efficiency and is defined as

$$\epsilon_\lambda^{\rm QE} = \frac{\text{number of electrons librated}}{\text{number of incident photons}} \qquad \text{counts photon}^{-1}. \tag{6.66}$$

The quantum efficiency is calibrated and published as a function of wavelength by the spectrograph design team or the manufacturer of the CCD and is usually made available by the observatory. However, since each pixel is an independent detector, there are small pixel to pixel variations in the quantum efficiency. The published quantum efficiency curve is the average of all pixels comprising the CCD.

In general, the number density flux of photons, n_λ [photon cm^{-2} sec^{-1} Å^{-1}], is the radiant flux density, F_λ [erg cm^{-2} sec^{-1} Å^{-1}], divided by the energy carried in the photons, hc/λ [erg photon^{-1}]. Thus, the number flux of photons incident on a pixel with width $\Delta\lambda_{\rm pix} = B_\lambda$ [Å pixel^{-1}] at wavelength λ is

$$\frac{dN_\lambda}{dt} = \dot{N}_\lambda = B_\lambda\, n_\lambda = B_\lambda\, F_\lambda^{(a)} \frac{\lambda}{hc} \qquad \text{photon cm}^{-2}\ \text{sec}^{-1}\ \text{pixel}^{-1}, \tag{6.67}$$

where $F_\lambda^{(a)}$ is the apparent flux (Eq. 6.52). It is possible that the flux can be time variable over the time interval of the observation; we will assume the flux is steady state.

To obtain the cumulative number of photons impinging on the pixel, we multiply $\dot{N}_\lambda$ by the time interval over which the photons were collected, Δt [sec], and the collecting area of the telescope, $A_{\rm T}$ [cm^2]. We then multiply this resulting number by the quantum efficiency of the CCD [counts photon^{-1}] in order to obtain the number of electrons liberated and stored in the pixel. We have

$$I_\lambda = \dot{I}_\lambda\, (A_{\rm T}\Delta t) = \epsilon_\lambda^{\rm QE}\, B_\lambda\, F_\lambda^{(a)} \frac{\lambda}{hc}\, (A_{\rm T}\Delta t) \qquad \text{counts pixel}^{-1}, \tag{6.68}$$

where $\dot{I}_\lambda$ is the count flux [counts cm^{-2} sec^{-1} pixels^{-1}].

As we have discussed above, the apparent flux is modified relative to the observed flux, F_λ, due to several wavelength dependent reflectivities and transmission, including the intensity function of the grating and degredation of the spectral purity (as given by the ISF). Summarizing, from source to detector, these modifications are:

1. attenuation/transmission of the atmosphere, $\epsilon_\lambda^{\rm A}$
2. efficiency/transmission of the telescope optics, $\epsilon_\lambda^{\rm T}$
3. light loss at the slit, $\epsilon_\lambda^{\rm S}$
4. efficiency/transmission of the collimator, $\epsilon_\lambda^{\rm C}$
5. efficiency/transmission and blaze function of the grating, $\epsilon_\lambda^{\rm G}$
6. degredation of the spectral purity, $\Phi_\lambda(\Delta\lambda)$
7. efficiency/transmission of the camera optics, $\epsilon_\lambda^{\rm O}$
8. quantum efficiency of the CCD, $\epsilon_\lambda^{\rm QE}$

where the various ϵ represent the transmission efficiencies (ratios of the flux following interaction with the medium or optical element to the flux before interaction). Accounting for all attenuations, the apparent flux incident on the detector is given by Eqs. 6.52 and 6.53 in the regions of absorption features and in the continuum, respectively.

Substituting Eq. 6.52 into Eq. 6.68, we obtain the electron counts per pixel in the detector mapped to wavelength λ in terms of the observed flux,

$$I_\lambda = \epsilon_\lambda^{\rm QE} B_\lambda\, \epsilon_\lambda^{\rm O} \Big\{ \Phi_\lambda(\Delta\lambda) \otimes \big[\epsilon_\lambda^{\rm G}\, \epsilon_\lambda^{\rm C}\, \epsilon_\lambda^{\rm T}\, \epsilon_\lambda^{\rm A}\, F_\lambda \big] \Big\} \frac{\lambda}{hc}\, (A_{\rm T} \Delta t)\,, \tag{6.69}$$

which applies in wavelength regions where accounting for the degredation of the spectral purity is important. Recall that in spectral regions where variations in the flux values are over wavelength scales much greater than the ISF resolution element (i.e., in the continuum, where $\tau_\lambda = 0$), we apply Eq. 6.53. The continuum electron counts per pixel are then

$$I_\lambda^c = \epsilon_\lambda^{\rm QE} B_\lambda\, \epsilon_\lambda^{\rm O}\, \epsilon_\lambda^{\rm G}\, \epsilon_\lambda^{\rm C}\, \epsilon_\lambda^{\rm T}\, \epsilon_\lambda^{\rm A}\, F_\lambda^0\, \frac{\lambda}{hc}\, (A_{\rm T} \Delta t)\,. \tag{6.70}$$

since the degredation of the spectral purity (convolution with the ISF) has negligible affect.

In the continuum of the source, we define the telescope throughput as

$$\epsilon(\lambda) = \epsilon_\lambda^{\rm QE}\, \epsilon_\lambda^{\rm O}\, \epsilon_\lambda^{\rm G}\, \epsilon_\lambda^{\rm C}\, \epsilon_\lambda^{\rm S}\, \epsilon_\lambda^{\rm T} = \frac{F_\lambda^c}{F_\lambda^0}\,. \tag{6.71}$$

The total throughput is the product $\epsilon(\lambda)\, \epsilon_\lambda^{\rm A}(z)$, where we have explicitely included the airmass dependence of the atmospheric attenuation due to the observation sightline angle, z, relative to the telescope zenith.

A typical telescope throughput curve, $\epsilon(\lambda)$, is illustrated in Figure 6.12*a*. A representative atmosphere attenuation curve for unity arimass is shown in Figure 6.12*b*. The solid curve is the transmission efficiency, $\epsilon_\lambda^{\rm A}$, which is the ratio of the flux entering the telescope to the observed flux incident on the atmosphere. The dashed line is the extinction in magnitudes, which is $-2.5 \log \epsilon_\lambda^{\rm A}$ (Hamuy et al., 1992).

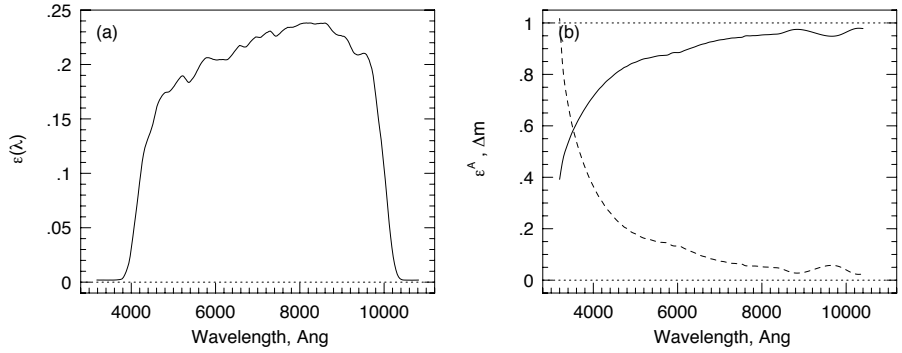

Figure 6.12: (*a*) A typical telescope throughput curve, $\epsilon(\lambda)$, for a hypothetical ground–based astronomical telescope and low–order optical spectrograph. Note that, at best, less than 25% of the observed flux reaches the detector. (*b*) The smoothed solid curve is the atmospheric transparency, $\epsilon^{\rm A}_\lambda(0)$, for unity airmass (toward the zenith). The dashed curve is the extinction in magnitudes, Δm.

The value $\epsilon(\lambda)$ is specific to the telescope and spectrograph. The value of $\epsilon^{\rm A}_\lambda(0)$ is dependent upon the elevation (altitude) of the observatory and can be affected by both atmospheric turbulence and the concetration of water vapor along the sightline to the object (quantities which are night to night variable). The observatory usually publishes these curves, where the atmospheric attenuation is for unity airmass averaged over many "photometric" nights (meaning negligible water vapor and minimal atmospheric turbulence). Once the electron counts from the source are measured, it is possible to recover the observed continuum flux, F^0_λ, using Eq. 6.70. This process is known as flux calibration, which we discuss further in § 7.5.

All subsequent discussion of the *detected* spectrum will refer to the electron counts, I_λ, and the continuum counts, $I^{\rm c}_\lambda$. As we shall see in future chapters, several noise sources result in some uncertainty in the measured counts. We will require keeping track of these noise sources in an effort to develop the error budget when we discuss analysis of the spectrum.

References

Filippenko, A. V. 1982, The importance of atmospheric differential refraction in spectrophotometry, *Pub. Astron. Soc. Pac.*, **94**, 715

Gray, D. F. 1992, *The Observational and Analysis of Stellar Photospheres*, Cambridge University Press

Hamuy, M., Walker, A. R., Suntzeff, N. B., Gigoux, P., Heathcote, S. R., &

Phillips, M. M. 1992, *Pub. Astron. Soc. Pac.*, Southern spectrophotometric standards, **104**, 533

Hecht, E. & Zajac, A. 1974, *Optics*, Addison Wesley

Schroeder, D. J. 1978, *Astronomical Optics*, Academic Press